JMEPEG (2024) 33:9028–9038
https://doi.org/10.1007/s11665-024-09486-4

1059-9495/$19.00

ORIGINAL RESEARCH ARTICLE

Mechanical and Electrochemical Properties Comparison of Additively Manufactured Ti-6Al-4V Alloys by Electron Beam Melting and Selective Laser Melting

Liliana Romero Reséndiz, Tonantzin Sánchez Cano, Muhammad Naeem, Asif Ur Rehman, Elmas Salamci, Vianey Torres Mendoza, Eduardo Degalez Duran, Lourdes Bazán Díaz, and Metin U. Salamci

Submitted: 7 December 2023 / Revised: 21 January 2024 / Accepted: 5 April 2024 / Published online: 30 April 2024

This work involves additively manufactured Ti-6Al-4V alloys, which are widely used in automobile, biomedical, and aircraft components for a comparison of the microstructure–properties relationship between electron beam melted (EBM) and selective laser melted (SLM) alloys after hot isostatic pressing treatment. We carried out microstructural, mechanical, and electrochemical measurements on both alloys. They showed comparable α and β phase contents with slightly higher lattice parameters in the EBM sample compared to the SLM. The EBM sample showed higher yield strength and uniform elongation due to the activation of multistage defects-driven strengthening and strain hardening mechanisms. Cracking during the tensile test nucleated mainly at the α phase near high-mechanical mismatch α/β interfaces. This mechanism was consistent with the reported generation of hetero-deformation-induced strengthening and strain hardening. Both alloys showed similar electrochemical behavior, but the SLM sample was more susceptible to corrosion than the EBM alloy.

Keywords additive manufacturing, biomaterial, corrosion, mechanical properties, microstructure, titanium alloy

1. Introduction

Additive manufacturing (AM) processing routes are advantageous over melting and conventional powder metallurgy due to precise microstructural control by modifying the processing parameters (Ref 1). Furthermore, AM allows large or small dimensional near-net-shapes production (Ref 2), which is a valuable attribute for producing devices of demanding geometry without requiring consecutive thermo-mechanical processes. AM also decreases heterogeneities such as segregation and inclusions, which are commonly found in cast metallic ingots (Ref 3, 4), thus requiring long-time homogenization heat treatments and altering the mechanical properties. On the other hand, the conventional wrought Ti alloys imply several melting cycles to overcome the purity shortcomings of the cast materials (Ref 5). The re-melting cycles are followed by thermo-mechanical routes as forging, milling and heat treatments, which increase the mechanical properties compared to casting components but also their production time (Ref 5). Besides processing advantages, microstructural control of AM-obtained materials may also result in a similar or improved electrochemical properties compared to cast counterparts (Ref 6, 7). Therefore, AM is one of the most promising fabrication techniques to produce metallic components (Ref 1, 2). Among several uses, biomedical implant development has greatly benefitted from AM due to its typical porous structures. Porosity triggers the anchorage of the implant to the organic tissue of bone (Ref 8-11).

Selective laser melting (SLM) and electron beam melting (EBM) are two AM techniques that have been widely studied and many of their processing parameters, such as scanning speed, beam power, hatch spacing, build direction, and beam spot size, are broadly understood (Ref 12, 13). SLM is based on the use of a focused laser beam to locally melt the powder bed and form layers onto a substrate (Ref 14). EBM uses an accelerated electronic beam to preheat and then melt the gravity-fed powder to produce melt pools and layers onto the substrate (Ref 14). The processing parameters of SLM and EBM are being well understood but a comparison of their properties in widely common alloys would be helpful to guide different industrial components development.

Liliana Romero Reséndiz, Departamento de Ingeniería Metalúrgica, Facultad de Química, Universidad Nacional Autónoma de México, 04510 Mexico City, Mexico; Department of Design and Engineering, Faculty of Science and Technology, Bournemouth University, Poole, Dorset BH12 5BB, UK; and School of Metallurgy and Materials, University of Birmingham, Birmingham B15 2TT, UK; **Tonantzin Sánchez Cano** and **Vianey Torres Mendoza**, Departamento de Ingeniería Metalúrgica, Facultad de Química, Universidad Nacional Autónoma de México, 04510 Mexico City, Mexico; **Muhammad Naeem**, School of Metallurgy and Materials, University of Birmingham, Birmingham B15 2TT, UK; **Asif Ur Rehman**, CY Advanced Studies, CY Cergy-Paris University, 95000 Paris, France; and Ermaksan, 16065 Bursa, Türkiye; **Elmas Salamci**, Department of Mechanical Engineering, Gazi University, 06570 Maltepe Ankara, Türkiye; **Eduardo Degalez Duran** and **Lourdes Bazán Díaz**, Instituto de Investigaciones en Materiales, Universidad Nacional Autónoma de México, Circuito exterior S/N, Cd. Universitaria, A. P. 70-360, CP 04510 Coyoacán, Mexico; and **Metin U. Salamci**, Department of Mechanical Engineering, Gazi University, 06570 Maltepe Ankara, Türkiye; and Additive Manufacturing Technologies Application and Research Center-EKTAM, Gazi University, 06980 Kahramankazan Ankara, Türkiye. Contact e-mail: m.naeem@bham.ac.uk.

Ti-6Al-4V alloy is the most popular alloy in the biomedical implant field, and it is also broadly used in automobile and aerospace components (Ref 15, 16). This is because of its adequate combination of mechanical properties, corrosion resistance, and biocompatibility (Ref 17, 18). Pitting corrosion does not generally occur in this alloy when exposed to amino acids or proteins (Ref 19-22). Therefore, the Ti-6Al-4V represents an accessible and widely used material for evaluating the properties achieved by SLM and EBM. Several aspects of electrochemical, mechanical, and biological properties adequacy for the abovementioned applications of the SLM- and EBM-produced Ti-6Al-4V have been reported (Ref 12, 18, 23, 24).

The Ti-6Al-4V alloys produced by SLM typically consist of lamellar martensite (α') and HCP (α) arrangements or lamellar α/α' + BCC (β), while the EBM commonly produces HCP (α) + BCC (β) microstructures (Ref 24, 25). Compared to SLM, the EBM alloy has been reported to show better performance with simulated body fluid under crevice corrosion and electrochemical corrosion at electrode potential higher than 1.5 V; however, it showed lower corrosion resistance during immersion test (Ref 23). A stable passive layer was observed in the more microstructurally homogeneous plane (Ref 25). The EBM sample showed lower corrosion resistance in NaCl solution due to micro-galvanic pairs formed at the multiphasic microstructure compared to the martensitic SLM microstructure (Ref 25).

Regarding mechanical properties, higher tensile strength and lower ductility were obtained from SLM Ti-6Al-4V than EBM (Ref 24). Both, strength and ductility were better in the vertically built (with respect to the substrate) orientation than in the horizontally built one in both SLM and EBM samples (Ref 24). Porosity decreased the fatigue strength of the AM samples compared to cast Ti-6Al-4V alloys. The effect of porosity on fatigue was reduced by using hot isostatic pressing (HIP) in both SLM and EBM alloys (Ref 24). Moreover, HIP improved the ductility of SLM Ti-6Al-4V alloy (Ref 26). In general, the reduction of metastable phases and stress relief through post-AM treatments has been widely reported as useful for improving the corrosion resistance of different alloys, including the Ti-6Al-4V (Ref 27, 28).

From the above, few comparisons of SLM and EBM have been carried out. Some reviews on AM techniques also discuss findings from SLM and EBM (Ref 2, 12, 14-16, 18, 29, 30). However, considering that they joined the state-of-the-art from different research groups with materials developed under several variables, e.g., chemical composition, environmental differences, different processing parameters, etc., those results may not be adequate to establish acceptable comparisons. Besides, apart from reporting the value of tensile properties, no analysis of the strain hardening rate has been done in comparative SLM and EBM Ti-6Al-4V works. So far, strain hardening has only been correlated to surface machinability during cutting processes (Ref 30). This analysis is important since it provides further information of the strengthening mechanisms, which is a key information to control and improved the design of alloys.

In this work, we performed a reliable comparison of EBM and SLM Ti-6Al-4V alloys with subsequent HIP treatment to further improve their mechanical behavior. We carried out microstructural, mechanical and electrochemical measurements to provide an in-depth microstructure–properties relationship with broad applicability to automobile, biomedical or aircraft Ti-6Al-4V components.

2. Experimental Procedure

2.1 Additive Manufacturing of Alloys

The SLM process was performed using an ENAVISION 250 ERMAKSAN LPBF machine equipped with a 500 W fiber laser and a build chamber under controlled atmospheric conditions. Ti-6Al-4V alloy powder with particle size from 15 to 45 μm was used as the feedstock material for AM. Flat Ti-6Al-4V alloy plates were used as the build platform. The laser power, scanning speed, spot size, and hatch distance of 200 W, 800 mm/s, 85, and 120 μm, respectively were used. Each layer was melted one by one and solidified successively. The EBM was performed in an ARCAM A2X additive manufacturing machine with vacuum environment. Ti-6Al-4V alloy powder with particle size distribution from 20 to 75 μm was utilized as primary feedstock material. The beam power of 1100 W and scanning speed of 6000 mm s^{-1} were used. Island scanning strategy was used to reduce residual stresses of the AM alloys (Ref 31). Each layer was melted one by one and solidified successively. The SLM and EBM alloys were subjected to HIP in a Quintus QIH-21 Hot Isostatic Pressing machine under 100 MPa at 920 °C for two hours according to the ASTM standard F3001 and then quenched with Argon at a cooling rate of around 20 and 25°C/min.

2.2 Microstructural, Mechanical and Electrochemical Assessment

The phase identification and the volume fraction estimation of HIP specimens were carried out by neutron diffraction measurements at the Takumi beamline of the Materials and Life Science Experimental Facility (MLF) at the Japan Proton Accelerator Research Complex (J-PARC). For microstructural characterization, samples were prepared by conventional metallography and polishing up to mirror-like appearance with 0.05 μm particle size alumina solution. Phase morphology and elemental distribution were analyzed by scanning electron microscopy (SEM) and energy-dispersive x-ray spectroscopy (EDS) in a JEOL 7600. Tensile specimens with gauge dimensions of 25 mm length, 4 mm width and 3 mm thickness were obtained by electric discharge machining. Samples were deformed at room temperature under uniaxial tensile loading at a strain rate of 10^{-3} s^{-1}. An extensometer was connected to samples during deformation to measure the elongation. Electrochemical polarization tests were carried out in a potentiostat-galvanostat Gill AC Instruments. Samples of 1 cm^2 were subjected to a solution of 3.5 wt.% NaCl prepared with NaCl of 98% purity. A sweep rate of 60 mV min^{-1} was used with − 500 and 500 mV as start and reverse potentials. A three-electrode system was used: a saturated Ag/AgCl electrode as the reference electrode, a graphite counter electrode, and the sample of Ti-6Al-4V as working electrode. The kinetic corrosion parameters were determined by using Tafel's extrapolation method. The corrosion parameters were fitted using EC-Lab software to determine the corrosion current (i_{corr}) and corrosion rate (CR) according to ASTM G102-89-2015. An equivalent weight of 11.768 g eq^{-1} and density of 4.43 g cm^{-3}

were considered for the CR calculations (Ref 32). All tests were performed three times to ensure reproducibility.

3. Results and Discussion

From SEM micrographs in Fig. 1, both EBM and SLM alloys are constituted of the same phases, i.e., α-HCP (hexagonal close-packed) and β-BCC (body-centered cubic). The dispersed lamellar β phase in both alloys is surrounded by the α matrix. Similar grain size and β dispersion can be observed in both alloys. Similar phase morphologies have already been reported in EBM Ti-6Al-4V (Ref 33), where α + β is transformed during cooling from the high temperature region of β. However, given the fast cooling during SLM typically produces α/α′ lamellar morphologies with columnar β phase (Ref 24). The similar phases and morphologies observed in Fig. 1 are the evidence of the near-equilibrium microstructures achieved after HIP. This is because the microstructure of AM Ti-6Al-4V is strongly dependent on the thermo-mechanical history (Ref 18).

EDS mapping and point analyses were done for both phases and the results are shown in Fig. 2 and Table 1. Vanadium (V) constituent element enriched the β phase, but it is depleted from the α phase in both alloys. An average increment of 29.9 and 42.5% more aluminum (Al) contents observed in the α phase than in the β phase of the EBM and SLM alloys, respectively. Contrastingly, titanium (Ti) seems equally distributed in both phases of EBM and SLM alloys. These results are in good agreement with the β- and α-stabilizing effect of V and Al, respectively (Ref 13). Other EBM alloys shown similar elemental distribution with V-enriched β phase and Al-enriched α phase (Ref 33).

To confirm the constituent phases and estimating their volume fractions, neutron diffraction measurements were carried out and the results are shown in Fig. 3 and Table 2. Both EBM and SLM samples consist of α-HCP and β-BCC phases. They were in comparable percentage in both alloys, i.e., 93.06 and 93.39% α while 6.94 and 6.61% β in the EBM and SLM samples, respectively. Moreover, the lattice parameters of phases in both samples confirm that they have similar chemical compositions, which agrees with the average elemental analysis from Table 1. The *a* and *c* lattice parameters of α-HCP phase have an increment of 0.08 and 0.008% in the EBM sample in comparison to the SLM sample. The slight increment of lattice parameters in the EBM sample is consistent with its higher contents of substitutional Al in the Ti-HCP matrix (Ref 34) (Table 1). While the α-HCP in the EBM samples has 12.6% Al, the SLM sample has 11.4%. The lattice parameter of the β-BCC phase in the SLM sample is quite similar to the EBM sample.

The tensile engineering stress–strain curves in Fig. 4(a) and the mechanical properties in Table 3 show a slightly higher yield strength (YS) and ultimate tensile strength (UTS) in the

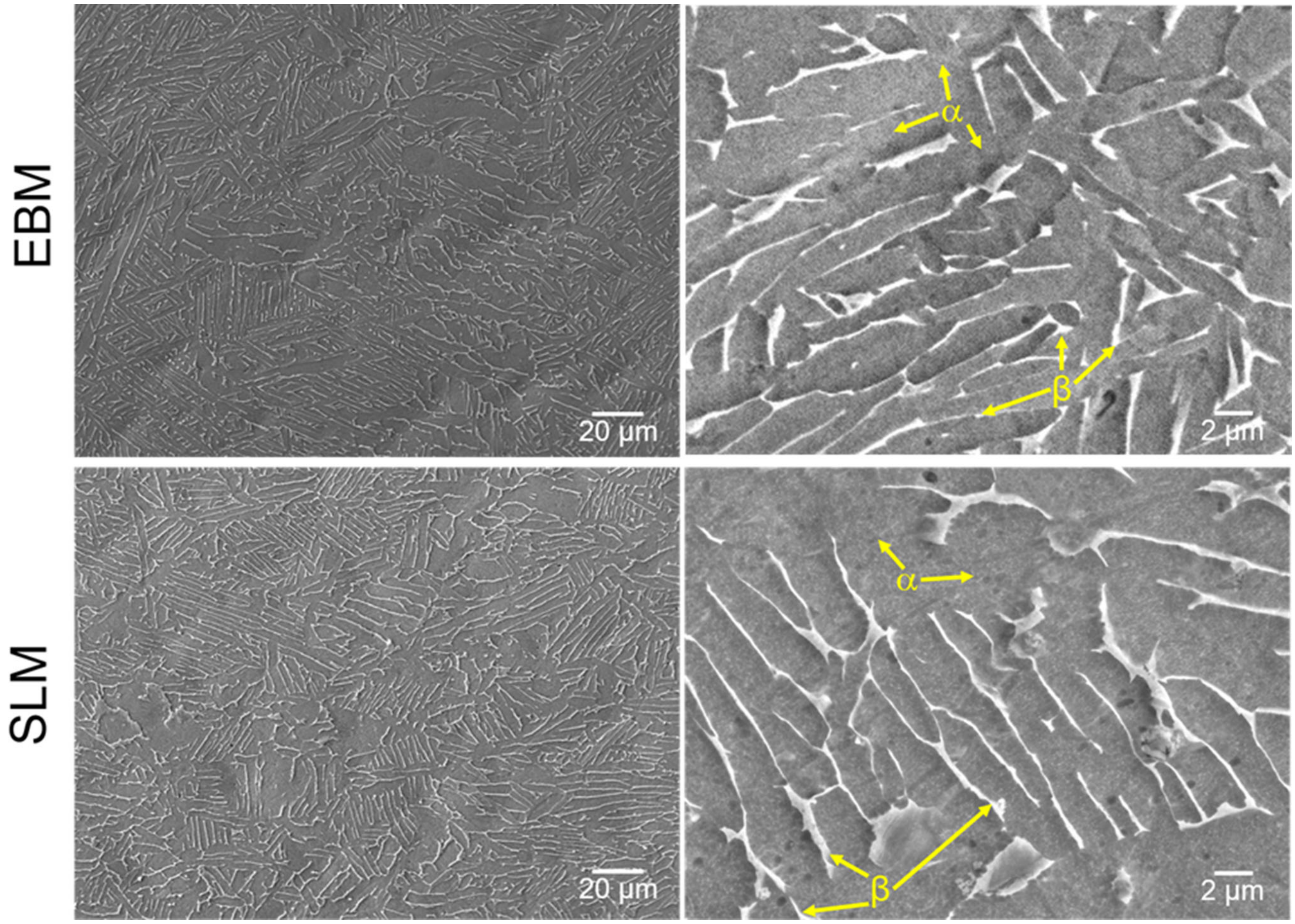

Fig. 1 SEM micrographs of EBM and SLM Ti-6Al-4V samples

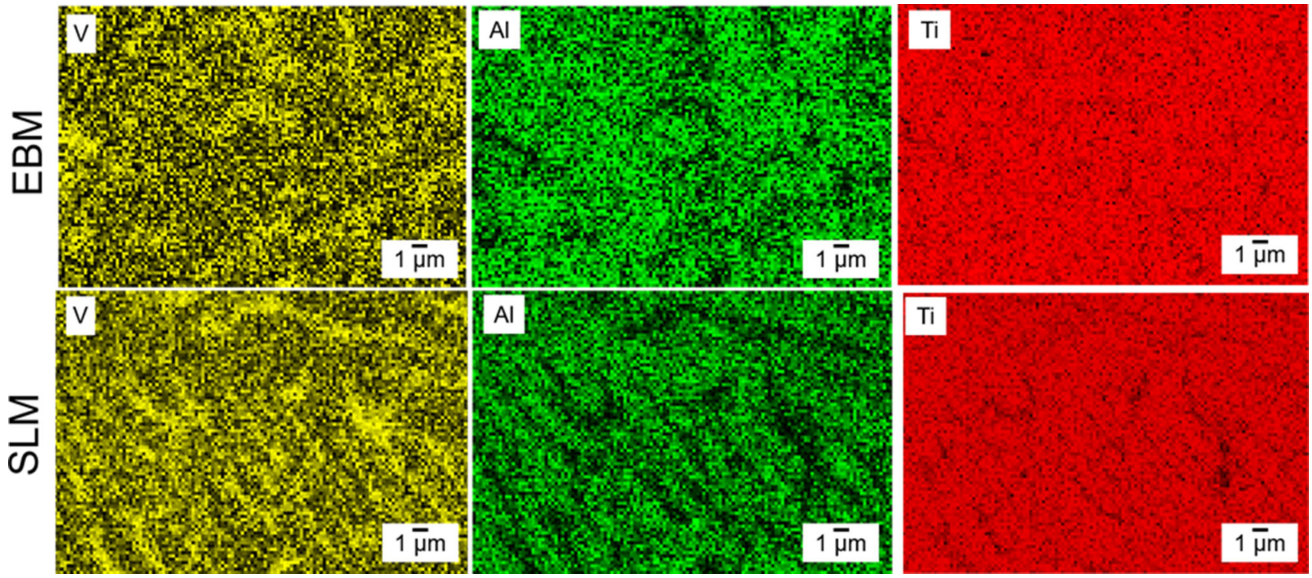

Fig. 2 EDS elemental mapping of EBM and SLM Ti-6Al-4V samples

Table 1 Qualitative EDS point analyses of EBM and SLM Ti-6Al-4V samples

	EBM			SLM		
Phase	**Ti**	**Al**	**V**	**Ti**	**Al**	**V**
α	87.4 ± 1.2	12.6 ± 1.2	0.0 ± 0.0	88.6 ± 0.9	11.4 ± 0.9	0.0 ± 0.0
β	89.5 ± 2.5	9.7 ± 1.1	0.9 ± 0.1	90.0 ± 4.2	8.0 ± 0.3	2.0 ± 0.1

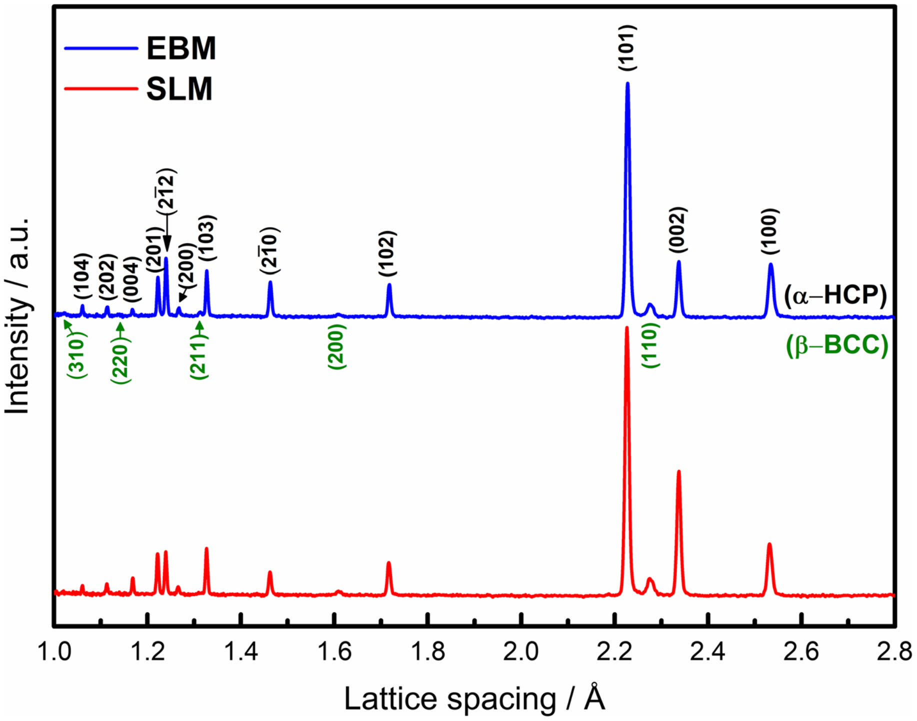

Fig. 3 Neutron diffraction patterns for EBM and SLM Ti-6Al-4V samples. The reflections for α-HCP and β-BCC phase are marked in green and black color, respectively

EBM alloy (936 and 1004 MPa) compared to the SLM one (921 and 996 MPa). Moreover, EBM has 38.8 and 40.6% higher uniform and total elongation with respect to the SLM alloy. Considering the comparable microstructure for both alloys given by similar grain size, phase dispersion and phase morphology shown in Fig. 1, their different tensile behavior may be related to the sole observed difference, i.e., lattice parameter (Table 2). The slightly higher YS and UTS in the EBM alloy with the larger lattice parameter agrees with the well-known solid solution hardening effect. However, lower ductility may be also expected (Ref 35), which corresponds to the strength-ductility trade-off of conventional metallic materials. Therefore, the larger uniform elongation in the EBM alloy suggests the existence of multiple strengthening mechanisms that may activate in a multistage trend to increase the strain hardening rate of the EBM alloy. This suggestion is also congruent with the nearly constant engineering stress after the YS, i.e., necking delay.

Table 2 Comparison of phase contents and lattice parameters calculated from neutron diffraction data of EBM and SLM Ti-6Al-4V samples

	EBM		SLM	
	α	β	α	β
Phase content, %	93.06	6.94	93.39	6.61
Lattice parameters, Å	a = 2.9256 c = 4.6731	3.2176	a = 2.9232 c = 4.6727	3.2177

Figure 4(b) shows strain hardening rate curves with respect to true strain. An activation of multi-stage defect-driven strengthening mechanisms can be observed in EBM sample from the two crests that provide secondary and tertiary risings of the strain hardening rate with increasing strain (Ref 36). Similar multistage strengthening behavior has been found in metallic materials with lamellar morphology (Ref 37). The defects observed from Fig. 1, 2 and 3 are substitutional atoms, multiphasic interfaces, and grain boundaries, to which the dislocations that allow plastic deformation in alloys can be added. The capacity of each defect to either increase the critical resolved shear stress or to promote dislocation accumulation will define their behavior as strengthening or strain hardening mechanisms, respectively. Some defects can also have a dual strengthening and strain hardening behavior (Ref 38, 39).

Besides the abovementioned defects, zone boundaries, i.e., high-mechanical mismatch at α/β interfaces, can also be expected (Ref 40). As any of the other defects, zone boundaries are also expected to interact with dislocations. The α-HCP phase has been proven to have a higher hardness than the β-BCC phase in Ti-6Al-4V (Ref 41). The high mechanical mismatch at zone boundaries induce the formation of a high density of geometrically necessary dislocation (GND) pile ups at the softer zone (β-BCC phase), which starts deforming before the harder zone, to accommodate the strain gradient near the interface (Ref 40). The presence of a high density of GND has been established in a deformed α/β Ti-6Al-4V, where the GNDs tend to be close to the grain boundaries (Ref 42). The GNDs cooperatively produce long-range stress (back stress), which is opposite to the applied shear stress, that limit the

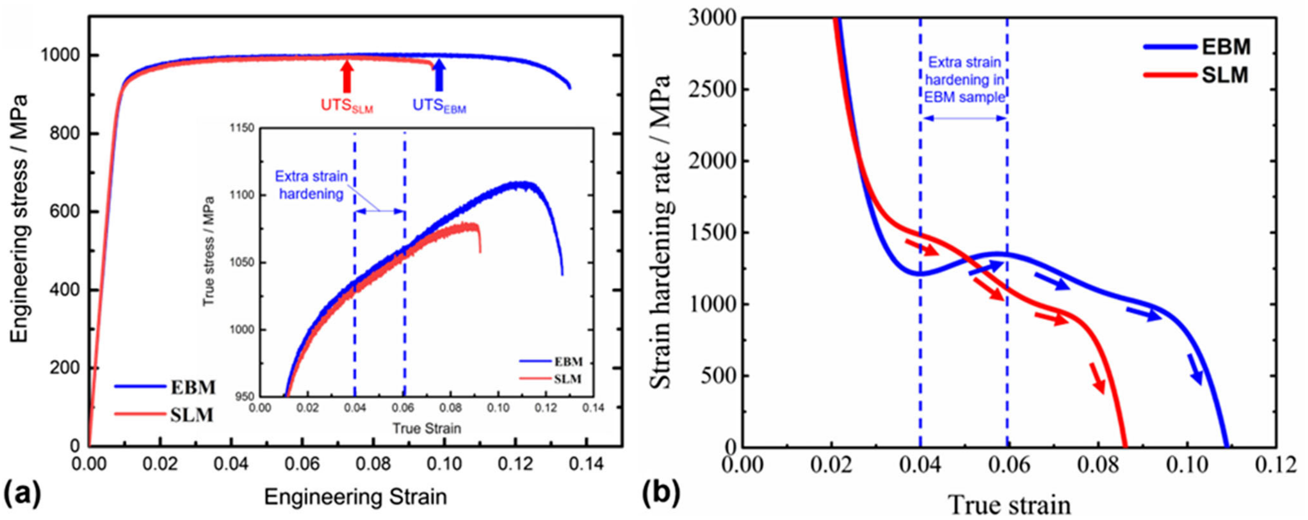

Fig. 4 (a) Engineering stress–strain and (b) strain hardening rate curves of EBM and SLM alloys

Table 3 Mechanical properties obtained from tensile test of EBM and SLM alloys

	YS, MPa	UTS, MPa	Uniform elongation, %	Total elongation, %	*E*, GPa
EBM	936	1004	9.9	13.5	111
SLM	921	996	7.3	9.6	115

emission of more dislocations from the source (Ref 40). Therefore, an increment of the critical resolved shear stress together with the back stress require higher applied stress to continue the plastic deformation, providing strengthening to the softer zone (β-BCC phase). On the other hand, the stress concentration given by the head of the GND pile up in the softer zone against the zone boundary has a magnitude proportional to the number of GNDs in the pile up. This generates a long-range stress at the harder zone, called forward stress, which promotes its deformation. Thus, the forward stress acts as an applied stress to promote dislocation slip (deformation) that promotes strain hardening in the harder zone. As back and forward stress have different distribution profiles from the zone boundary to the grain interior, they do not cancel each other and together give rise to hetero-deformation induced (HDI) stress (Ref 40). At high strain, the zone with the lowest plasticity, i.e., the harder zone, is expected to fail before the soft zone. This phenomenon has been observed in a B2-precipitate bearing high entropy alloy, where cracking nucleated at the harder B2 precipitates near the phase interface (Ref 37). Therefore, the high mechanical mismatch at soft/hard interfaces are the preferred cracking site due to stress concentrators (Ref 40). Figure 5 shows preferential cracking formation at the α phase nucleated near the α/β interfaces.

From the above, HDI acts dually as strengthening and strain hardening mechanism. Similar effect has been reported in other Ti-6Al-4V where the interface area per unit volume increased at higher annealing temperature and the strain hardening rate shows a slower reduction rate different from the typical banana-like curve (Ref 41). This behavior was also visible in the stress–strain curve curves where the uniform elongation increased at the same annealing temperatures that show the slowest decrement of strain hardening rate (Ref 41). Hence, the extra strain hardening rate observed from 0.04 to 0.06 true strain in the EBM sample (Fig. 4b) may be attributed to the HDI strain hardening. Similar rising of strain hardening rate due to HDI strain hardening has been reported in other materials with lamellar morphology (Ref 37). From the literature (Ref 37), as in the EBM sample of the current work, the dual strengthening and strain hardening effects originated from the HDI stress, allowed achieving higher YS and uniform elongation synergistically (Table 3). The reason for the EBM to show higher HDI compared to the SLM may be related to the only structural difference, i.e., higher α lattice parameters in the EBM sample compared to the SLM alloy (Fig. 3 and Table 2). As explained before, the higher lattice parameter may be related to a more significant hardening effect from the higher contents of substitutional Al atoms in the α matrix. Thus, the higher lattice

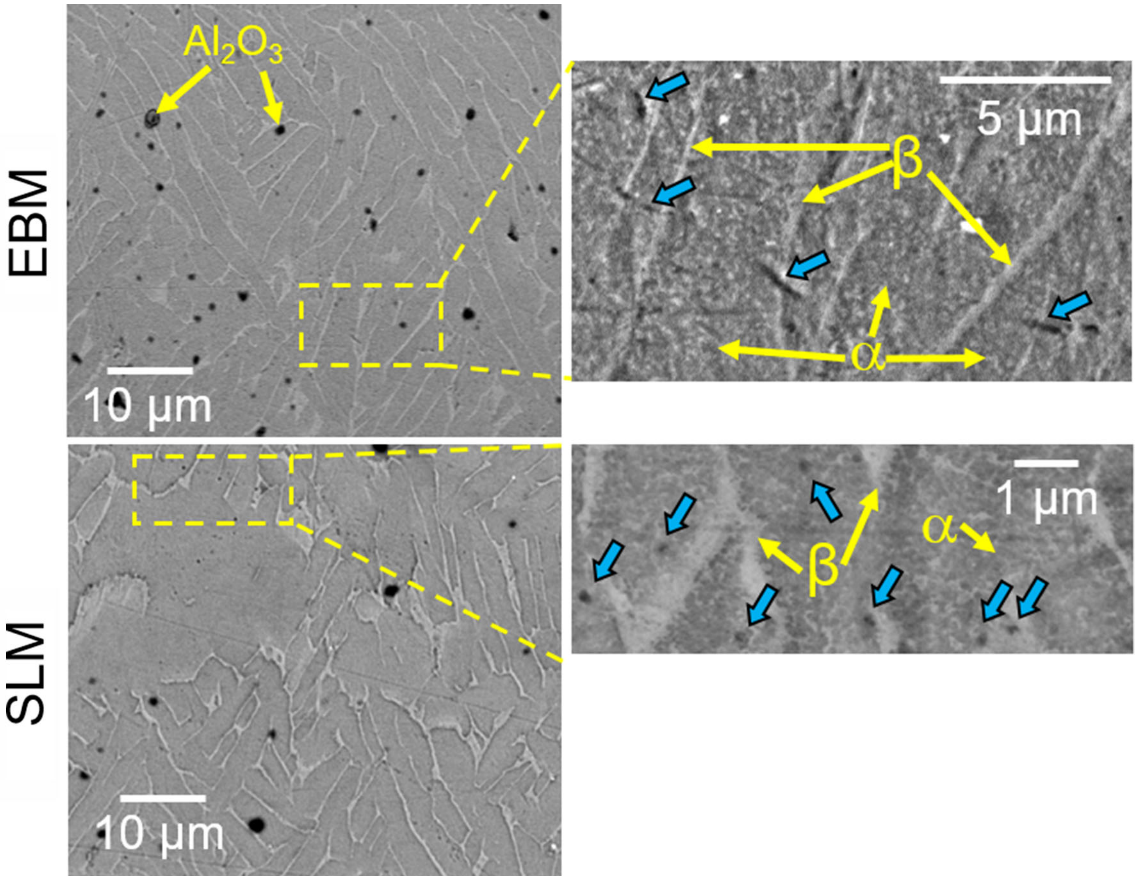

Fig. 5 SEM micrographs of EBM and SLM samples showing crack nucleation (blue arrows) preferentially at the α phase (near phase interfaces). Al_2O_3 presence is due to the contamination during polishing (Color figure online)

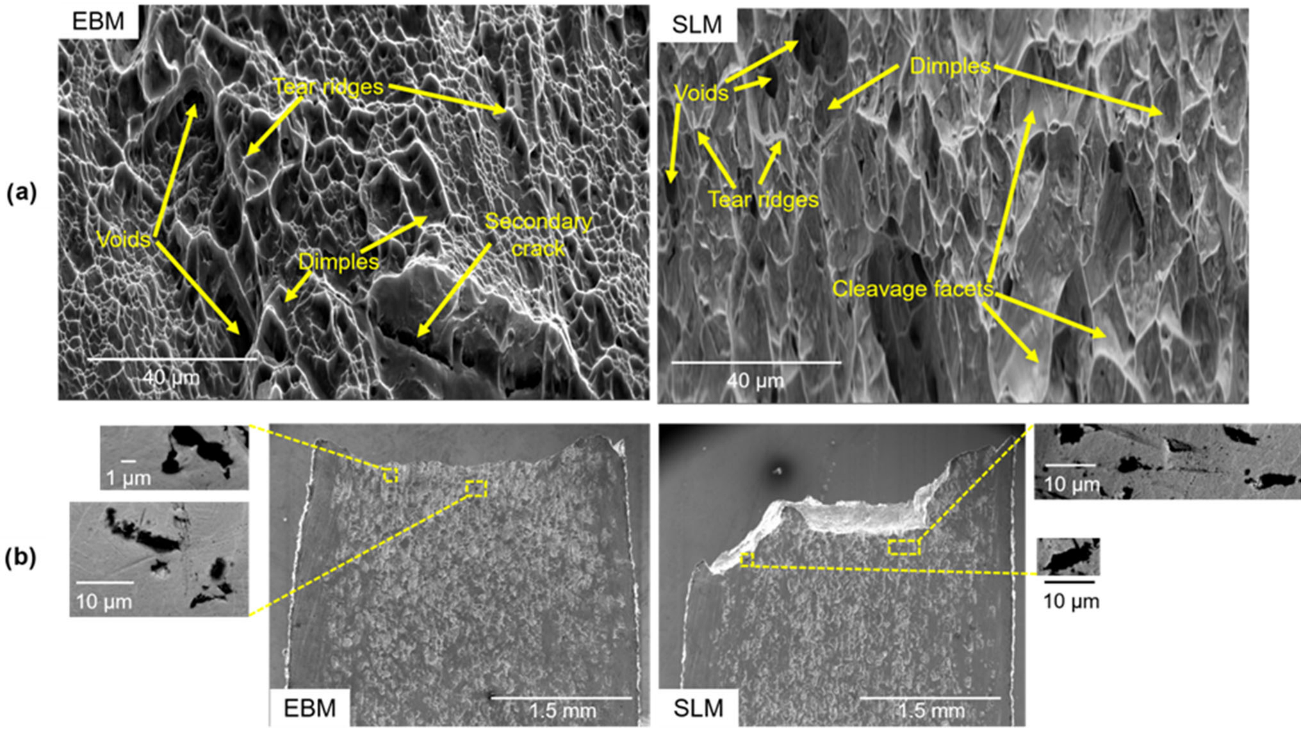

Fig. 6 SEM micrographs after tensile test showing the (a) fracture surface in the transversal plane and (b) the fracture patterns in the longitudinal plane of EBM and SLM samples

misfit between α and β phases in the EBM sample may be accommodated by higher HDI stress.

Figure 6(a) shows the fractured surfaces of the EBM and SLM samples to observe the correlation between the tensile deformation and fracture behavior. The fracture of the EBM sample is homogeneously dominated by dimples, which are related to a plastic fracture behavior (Ref 43). Tear ridges, cleavage facets and a lower number of dimples suggested a quasi-cleavage fracture in the SLM sample due to its lower tensile plasticity compared to the EBM sample (Ref 43). Combined plastic and brittle like fracture behaviors have been reported in SLM Ti-6Al-4V alloys (Ref 44). The same report showed a dimple-dominated plastic fracture behavior in the EBM Ti-6Al-4V alloy (Ref 44). HIP treatment applied to SLM Ti-6Al-4V samples have been effectively shown to reduce the number of voids (Ref 45), which may be related to their lower number in both alloys. Those voids could act as crack initiators as they are expected to form at defects, i.e., stress concentrators, that localized the strain during the tensile loading (Ref 46). Increasing plastic deformation prompts void growth and coalesce, which forms larger defects and leads to fracture (Ref 46). Void-driven cracking is shown in Fig. 6(b), where void coalescence is evidenced in both studied SLM and EBM samples.

Apart from mechanical properties, chemical properties, such as corrosion may also be sensitive to the effect of elemental distribution. To evaluate electrochemical behavior, potentiodynamic polarization testing was performed on both EBM and SLM alloys (Fig. 7a). The kinetic parameters derived from the curves are given in Table 4, where E_{corr} is the corrosion potential, βc and βa are cathodic and anodic slope respectively, and i_{corr} is the corrosion current density derived from the Tafel extrapolation technique. The polarization behavior of both alloys shows similar polarization performance. The appearing of a limiting current density in the cathodic region suggest it to be controlled by oxygen-diffusion (Ref 47). This agrees with the more negative cathodic slope of the EBM ($-$ 0.291 V dec^{-1}) compared to that of the SLM ($-$ 0.229 V dec^{-1}), which indicates that the oxygen reduction reaction is kinetically favored in the EBM. The anodic region presents an active-passive behavior (a passivation process) given by a formation of the surface oxide layer. The morphology of the surface passivation layer of both alloys is comparable and is mainly formed by homogeneous flake-like layers of TiO_2 and some globular Al_2O_3 particles (Fig. 8). These results are in agreement with the reported oxide layer for Ti-6Al-4V alloys mainly constituted of TiO_2 and Al_2O_3 (Ref 48, 49).

The corrosion potential (E_{corr}) of EBM and SLM alloys are $-$ 0.351 and $-$ 0.345 V, respectively. These values are less negative than those reported for various Ti-6Al-4V alloys, all tested in NaCl solution (Fig. 7b), indicating the lower electrochemical activity due to a more stable passive layer. Lamellar grain morphologies (like those obtained in the EBM and SLM samples) are reported with better uniform corrosion resistance compared to other morphologies like coarse and equiaxed grain morphologies tested in NaCl (Ref 50). Therefore, demonstrating a better corrosion resistance of the EBM and SLM alloys of this work. The standard deviations of potential and current are slightly larger for the SLM sample than that of EBM, which could be attributed to a higher activity in the SLM sample and therefore a greater activity in the formation of the passive film. That is why SLM exhibits a higher i_{corr} and higher corrosion rate (CR) than the EBM sample. This may be related to the microstructural differences between the two alloys, i.e., higher lattice misfit between α and β phases in the EBM sample caused by the higher contents of substitutional Al atoms in its α matrix (Table 1 and 2). Al additions in Ti-alloys have been reported to decrease CR (Ref 51). Thus, the dominant phase in the EBM alloy, i.e., α phase, may have lower corrosion than that in the SLM alloy. However, a systematic study of the effect of Al additions in the Ti-6Al-4V alloy is recommended to establish this hypothesis. Regardless of the differences between both alloys, their corrosion rates are feasible for multiple industrial applications as they are lower than that recommended by the American Association of Corrosion Engineers of 0.05 mm year^{-1} (Ref 23). Additionally, the CR can be considered as perfect ($< 10^{-3}$ mm year^{-1}) and very stable (10^{-3}-10^{-2} mm year^{-1}) for the EBM and SLM samples, respectively (Ref 50).

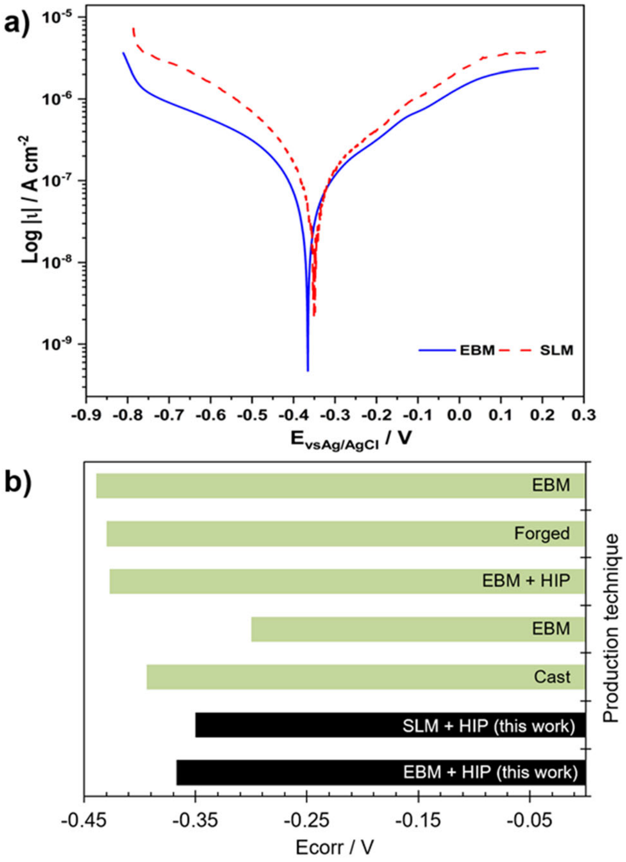

Fig. 7 Corrosion behavior by (a) potentiodynamic curves and (b) comparison of corrosion potential of EBM and SLM alloys of this work with Ti-6Al-4V alloys from literature (Ref 33, 48, 52)

4. Conclusions

The electron beam melted (EBM) and selective laser melted (SLM) Ti-6Al-4V alloys after hot isostatic pressing shown higher ductility compared to their reported EBM and SLM counterparts in as-printed state. The microstructure–properties relationship was studied by electron microscopy as well as tensile and electrochemical polarization testing. The main findings can be summarized as follows:

1. Both alloys showed similar microstructures described by lamellar V-enriched β-BCC phase surrounded by Al-enriched α-HCP phase. The phase percentage of 93.06 and 93.39% α-phase was comparable for both alloys. A slight increment of lattice parameters in the EBM sample was consistent with its higher content of substitutional Al in the α-HCP matrix.
2. The EBM sample showed simultaneously 1% higher yield strength and 39% higher uniform elongation than the SLM alloy. The strain hardening rate curve of the EBM sample showed extra strain hardening given by the activation of multistage defects-driven strengthening and strain hardening mechanisms, i.e., substitutional solid solution, multiphasic interfaces, grain boundaries, and zone boundaries.
3. Dimple dominated fracture surface in the EBM sample was congruent with its higher plasticity compared to the SLM sample, which showed a combined plastic and brittle like fracture behavior.
4. Cracking nucleated mainly at the α phase near high-mechanical mismatch α/β interfaces. This mechanism was consistent with the reported generation of hetero-deformation-induced (HDI) strengthening and strain hardening. The HDI may be boosted in the EBM sample due to the higher lattice misfit between its phases.
5. The EBM and SLM samples presented similar electrochemical activity evolution consistent with a similar microstructure and chemical composition. A slightly higher corrosion rate of the SLM sample may be related to the lower Al content in its matrix compared to that in the EBM sample.

Table 4 Electrochemical parameters from potentiodynamic curves of both studied alloys

Alloy	E_{corr}, V	βc, V dec^{-1}	βa, V dec^{-1}	i_{corr}, μA cm^{-2}	CR, μm year^{-1}
EBM	-0.351 ± 0.016	-0.291 ± 0.019	0.332 ± 0.025	0.088 ± 0.179	0.744 ± 1.15
SLM	-0.345 ± 0.023	-0.229 ± 0.027	0.212 ± 0.044	0.165 ± 0.286	1.396 ± 1.98

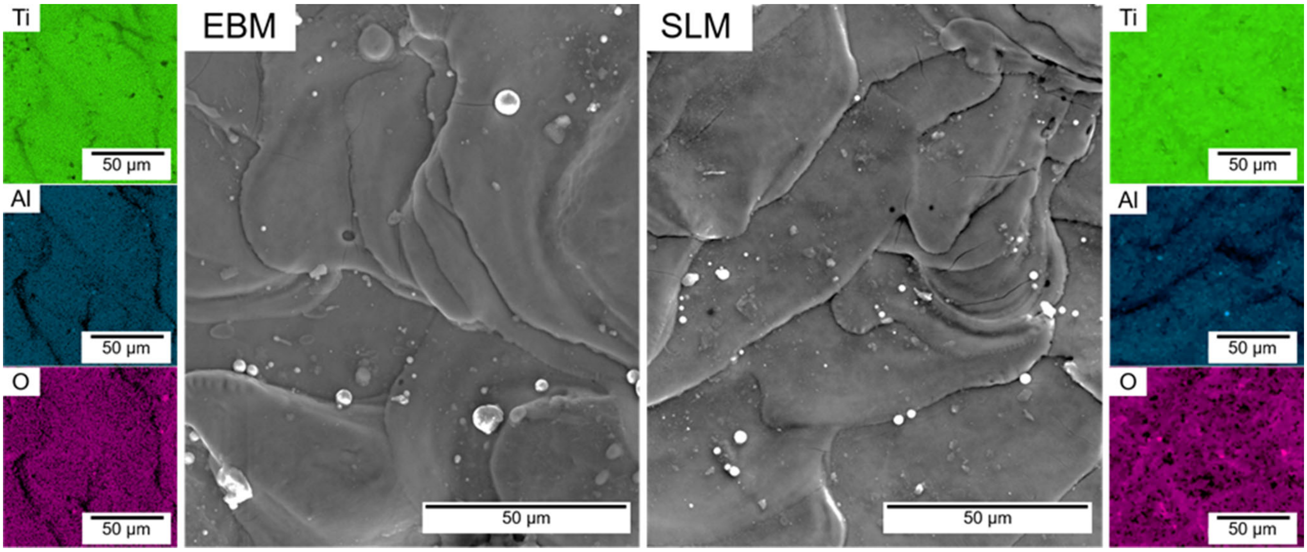

Fig. 8 EDS mapping of surface corrosion products of EBM and SLM samples

Acknowledgments

This work was funded by the Scientific and Technological Research Council of Turkiye-TUBITAK under 1004 platform program for the "New Generation 3D Printing Manufacturing Technologies Platform" [Grant Number: 20AG008], the Programa de Apoyo a la Investigación y el Posgrado of Universidad Nacional Autónoma de México (UNAM) [PAIP-50009223]; the Programa de Apoyo a Proyectos de Investigación e Innovación Tecnológica, UNAM [PAPIIT-IA102724]. M. Naeem thanks the Asia-Oceania Neutron Scattering Association (AONSA) for the award of the AONSA Young Research Fellowship [AONSA-YRF-2022]. The authors acknowledge the support from Eliezer Hernández Mecinas for tensile testing. The neutron diffraction experiments were performed at TAKUMI in MLF of J-PARC Center under the proposal number 2022B0140.

Author Contributions

L. Romero-Resendiz contributed to funding acquisition, visualization, formal analysis, writing-original draft. T. Sánchez-Cano contributed to methodology and formal analysis. M. Naeem contributed to supervision, methodology, formal analysis, project administration, writing—review and editing. A.U. Rehman contributed to methodology, writing—review and editing. E. Salamci contributed to writing—review and editing. V. Torres-Mendoza contributed to resources, writing—review and editing. E. Degalez-Duran and L. Bazán-Díaz contributed to methodology. M.U. Salamci contributed to resources.

Data Availability

The raw data related to this manuscript would be made available on request.

Conflict of interest

The authors declare that there are no conflict of interest.

Open Access

References

1. A. Saboori, D. Gallo, S. Biamino, P. Fino, and M. Lombardi, An Overview of Additive Manufacturing of Titanium Components by Directed Energy Deposition: Microstructure and Mechanical Properties, *Appl. Sci.*, 2017, **7**(9), p 883–906
2. W.E. Frazier, Metal Additive Manufacturing: A Review, *J. Mater. Eng. Perform.*, 2014, **23**(6), p 1917–1928
3. H.B. Bomberger and F.H. Froes, The Melting of Titanium, *JOM*, 1984, **36**(12), p 39–47
4. A. Mitchell, Melting, Casting and Forging Problems in Titanium Alloys, *Mater. Sci. Eng. A*, 1998, **243**(1–2), p 257–262
5. L.E. Murr, S.A. Quinones, S.M. Gaytan, M.I. Lopez, A. Rodela, E.Y. Martinez, D.H. Hernandez, E. Martinez, F. Medina, and R.B. Wicker, Microstructure and Mechanical Behavior of Ti-6Al-4V Produced by Rapid-Layer Manufacturing, for Biomedical Applications, *J. Mech. Behav. Biomed. Mater.*, 2009, **2**(1), p 20–32. https://doi.org/10.1016/j.jmbbm.2008.05.004
6. A. Leon, A. Shirizly, and E. Aghion, Corrosion Behavior of AlSi10Mg Alloy Produced by Additive Manufacturing (AM) vs. Its Counterpart Gravity Cast Alloy, *Metals (Basel)*, 2016, **6**(7), p 148
7. M.A. Melia, H.D.A. Nguyen, J.M. Rodelas, and E.J. Schindelholz, Corrosion Properties of 304L Stainless Steel Made by Directed Energy Deposition Additive Manufacturing, *Corros. Sci.*, 2019, **152**, p 20–30
8. S. Ponader, C. Von Wilmowsky, M. Widenmayer, R. Lutz, P. Heinl, C. Körner, R.F. Singer, E. Nkenke, F.W. Neukam, and K.A. Schlegel, In

Vivo Performance of Selective Electron Beam-Melted Ti-6Al-4V Structures, *J. Biomed. Mater. Res. Part A*, 2010, **92**(1), p 56–62

9. G.A.W. Murray and J.C. Semple, Transfer of Tensile Loads from a Prosthesis to Bone Using Porous Titanium, *J. Bone Jt. Surg.*, 1981, **63B**(1), p 138–141
10. M. Bram, T. Ebel, M. Wolff, A.P. Cysne Barbosa, and N. Tuncer, Applications of Powder Metallurgy in Biomaterials, *Advances in Powder Metallurgy*. I. Chang, Y. Zhao Ed., Woodhead Publishing, Sawston, 2013, p 520–554
11. T.S. Goia, K.B. Violin, M. Yoshimoto, J.C. Bressiani, and A.H.A. Bressiani, Osseointegration of Titanium Alloy Macroporous Implants Obtained by PM with Addition of Gelatin, *Adv. Sci. Technol.*, 2010, **76**, p 259–263
12. H.M. Khan, G. Özer, M.S. Yilmaz, and E. Koc, Corrosion of Additively Manufactured Metallic Components: A Review, *Arab. J. Sci. Eng.*, 2022, **47**(5), p 5465–5490. https://doi.org/10.1007/s13369-021-06481-y
13. H.M. Hamza, K.M. Deen, A. Khaliq, E. Asselin, and W. Haider, Microstructural, Corrosion and Mechanical Properties of Additively Manufactured Alloys: A Review, *Crit. Rev. Solid State Mater. Sci.*, 2022, **47**(1), p 46–98. https://doi.org/10.1080/10408436.2021.1886044
14. L.E. Murr, S.M. Gaytan, D.A. Ramirez, E. Martinez, J. Hernandez, K.N. Amato, P.W. Shindo, F.R. Medina, and R.B. Wicker, Metal Fabrication by Additive Manufacturing Using Laser and Electron Beam Melting Technologies, *J. Mater. Sci. Technol.*, 2012, **28**(1), p 1–14. https://doi.org/10.1016/S1005-0302(12)60016-4
15. T.S. Tshephe, S.O. Akinwamide, E. Olevsky, and P.A. Olubambi, Additive Manufacturing of Titanium-Based Alloys—A Review of Methods, Properties, Challenges, and Prospects, *Heliyon*, 2022, **8**(3), e09041. https://doi.org/10.1016/j.heliyon.2022.e09041
16. H.D. Nguyen, A. Pramanik, A.K. Basak, Y. Dong, C. Prakash, S. Debnath, S. Shankar, I.S. Jawahir, S. Dixit, and D. Buddhi, A Critical Review on Additive Manufacturing of Ti-6Al-4V Alloy: Microstructure and Mechanical Properties, *J. Mater. Res. Technol.*, 2022, **18**, p 4641–4661. https://doi.org/10.1016/j.jmrt.2022.04.055
17. B.G. Pound, Corrosion Behavior of Metallic Materials in Biomedical Applications. I. Ti and Its Alloys, *Corros. Rev.*, 2014, **32**(1–2), p 1–20
18. S.L. Sing, J. An, W.Y. Yeong, and F.E. Wiria, Laser and Electron-Beam Powder-Bed Additive Manufacturing of Metallic Implants: A Review on Processes, Materials and Designs, *J. Orthop. Res.*, 2016, **34**(3), p 369–385
19. R.J. Solar, S.R. Pollack, and E. Korostoff, In Vitro Corrosion Testing of Titanium Surgical Implant Alloys: An Approach to Understanding Titanium Release from Implants, *J. Biomed. Mater. Res.*, 1979, **13**(2), p 217–250
20. Y. Nakayama, T. Yamamuro, Y. Kotoura, and M. Oka, In Vivo Measurement of Anodic Polarization of Orthopaedic Implant Alloys: Comparative Study of in Vivo and in Vitro Experiments, *Biomaterials*, 1989, **10**(6), p 420–424
21. D.C. Hansen, The Effect of a Novel Biopolymer on the Corrosion of 316L Stainless Steel and Ti6Al4V Alloys in A Physiologically Relevant Electrolyte, *Corrosion*, 2007, NACE-07677
22. K.M. Speck and A.C. Fraker, Anodic Polarization Behavior of Ti-Ni and Ti-6A 1–4 V in Simulated Physiological Solutions, *J. Dent. Res.*, 1980, **59**(10), p 1590–1595
23. B. Zhao, H. Wang, N. Qiao, C. Wang, and M. Hu, Corrosion Resistance Characteristics of a Ti-6Al-4V Alloy Scaffold That Is Fabricated by Electron Beam Melting and Selective Laser Melting for Implantation in Vivo, *Mater. Sci. Eng. C*, 2017, **70**, p 832–841. https://doi.org/10.1016/j.msec.2016.07.045
24. X. Zhao, S. Li, M. Zhang, Y. Liu, T.B. Sercombe, S. Wang, Y. Hao, R. Yang, and L.E. Murr, Comparison of the Microstructures and Mechanical Properties of Ti-6Al-4V Fabricated by Selective Laser Melting and Electron Beam Melting, *Mater. Des.*, 2016, **95**, p 21–31. https://doi.org/10.1016/j.matdes.2015.12.135
25. P. Metalnikov, G. Ben-Hamu, and D. Eliezer, Corrosion Behavior of AM-Ti-6Al-4V: A Comparison between EBM and SLM, *Prog. Addit. Manuf.*, 2022, **7**(3), p 509–520. https://doi.org/10.1007/s40964-022-00293-8
26. C. Qiu, N.J.E. Adkins, and M.M. Attallah, Microstructure and Tensile Properties of Selectively Laser-Melted and of HIPed Laser-Melted Ti-6Al-4V, *Mater. Sci. Eng. A*, 2013, **578**, p 230–239. https://doi.org/10.1016/j.msea.2013.04.099
27. A. Biserova-Tahchieva, M.V. Biezma-Moraleda, N. Llorca-Isern, J. Gonzalez-Lavin, and P. Linhardt, Additive Manufacturing Processes in Selected Corrosion Resistant Materials: A State of Knowledge Review, *Materials (Basel)*, 2023, **16**(5), p 1893
28. C. Örnek, Additive Manufacturing—A General Corrosion Perspective, *Corros. Eng. Sci. Technol.*, 2018, **53**(7), p 531–535. https://doi.org/10.1080/1478422X.2018.1511327
29. P.K. Gokuldoss, S. Kolla, and J. Eckert, Additive Manufacturing Processes: Selective Laser Melting, Electron Beam Melting and Binder Jetting-Selection Guidelines, *Materials (Basel)*, 2017, **10**(6), p 672
30. N. Uçak, A. Çiçek, and K. Aslantas, Machinability of 3D Printed Metallic Materials Fabricated by Selective Laser Melting and Electron Beam Melting: A Review, *J. Manuf. Process.*, 2022, **80**, p 414–457. https://doi.org/10.1016/j.jmapro.2022.06.023
31. V. Kumar, B.R. Isanaka, S. Gupta, and V. Kushvaha, *Future Trends and Technologies in Additive and Substractive Manufacturing*, Springer Series in Advanced Manufacturing. Springer, Singapore, 2021
32. S. Cecchel, L. Montesano, and G. Cornacchia, Wear and Corrosion Characterization of a Ti–6Al–4V Component for Automotive Applications: Forging versus Selective Laser Melting Technologies, *Adv. Eng. Mater.*, 2022, **24**(8), p 1–10
33. L. Romero-Resendiz, M.C. Rossi, A. Alvarez, A. García-García, L. Milian, M.A. Tormo-Mas, and V. Amigo-Borras, Microstructural, Mechanical, Electrochemical, and Biological Studies of an Electron Beam Melted Ti-6Al-4V Alloy, *Mater. Today Commun.*, 2022, **31**, p 103337–103351
34. S. Sahoo, O. Licata, B. Mazumder, and S. Roy, Novel Insights on the Near Atomic Scale Spatial Distributions of Substitutional Alloying and Interstitial Impurity Elements in Ti-6Al-4V Alloy, *J. Alloys Compd.*, 2022, **907**, p 164511. https://doi.org/10.1016/j.jallcom.2022.164511
35. N. Hrabe and T. Quinn, Effects of Processing on Microstructure and Mechanical Properties of a Titanium Alloy (Ti-6Al-4V) Fabricated Using Electron Beam Melting (EBM), Part 2: Energy Input, Orientation, and Location, *Mater. Sci. Eng. A*, 2013, **573**, p 271–277. https://doi.org/10.1016/j.msea.2013.02.065
36. L. Romero-Resendiz, M. El-Tahawy, T. Zhang, M.C. Rossi, D.M. Marulanda-Cardona, T. Yang, V. Amigo-Borras, Y. Huang, H. Mirzadeh, I.J. Beyerlein, J.C. Huang, T.G. Langdon, and Y.T. Zhu, Heterostructured Stainless Steel: Properties, Current Trends, and Future Perspectives, *Mater. Sci. Eng. R*, 2022, **150**, 100691
37. P. Shi, Y. Zhong, Y. Li, W. Ren, T. Zheng, Z. Shen, B. Yang, J. Peng, P. Hu, Y. Zhang, P.K. Liaw, and Y. Zhu, Multistage Work Hardening Assisted by Multi-type Twinning in Ultrafine-Grained Heterostructural Eutectic High-Entropy Alloys, *Mater. Today*, 2020, **41**, p 62–71
38. X.L. Liu, Q.Q. Xue, W. Wang, L.L. Zhou, P. Jiang, H.S. Ma, F.P. Yuan, Y.G. Wei, and X.L. Wu, Back-Stress-Induced Strengthening and Strain Hardening in Dual-Phase Steel, *Materialia*, 2019, **7**, 100376
39. Z. An, S. Mao, Y. Liu, L. Yang, A. Vayyala, X. Wei, C. Liu, C. Shi, H. Jin, C. Liu, J. Zhang, Z. Zhang, and X. Han, Inherent and Multiple Strain Hardening Imparting Synergistic Ultrahigh Strength and Ductility in a Low Stacking Faulted Heterogeneous High-Entropy Alloy, *ACTA Mater.*, 2023, **243**, 118516. https://doi.org/10.1016/j.actamat.2022.118516
40. X.W. Yuntian Zhu, Heterostructured Materials, *Prog. Mater. Sci.*, 2023, **131**, 101019. https://doi.org/10.1016/j.pmatsci.2022.101019
41. Y. Chong, T. Bhattacharjee, M.H. Park, A. Shibata, and N. Tsuji, Factors Determining Room Temperature Mechanical Properties of Bimodal Microstructures in Ti-6Al-4V Alloy, *Mater. Sci. Eng. A*, 2018, **730**, p 217–222. https://doi.org/10.1016/j.msea.2018.06.019
42. P.D. Littlewood, T.B. Britton, and A.J. Wilkinson, Geometrically Necessary Dislocation Density Distributions in Ti-6Al-4V Deformed in Tension, *ACTA Mater.*, 2011, **59**(16), p 6489–6500. https://doi.org/10.1016/j.actamat.2011.07.016
43. Y.T. Zhu and X.L. Wu, Ductility and Plasticity of Nanostructured Metals: Differences and Issues, *Mater. Today Nano*, 2018, **2**, p 15–20
44. H.K. Rafi, N.V. Karthik, H. Gong, T.L. Starr, and B.E. Stucker, Microstructures and Mechanical Properties of Ti6Al4V Parts Fabricated by Selective Laser Melting and Electron Beam Melting, *J. Mater. Eng. Perform.*, 2013, **22**(12), p 3872–3883

45. P. Jamshidi, M. Aristizabal, W. Kong, V. Villapun, S.C. Cox, L.M. Grover, and M.M. Attallah, Selective Laser Melting of Ti-6Al-4V: The Impact of Post-processing on the Tensile, Fatigue and Biological Properties for Medical Implant Applications, *Materials (Basel)*, 2020, **13**(12), p 1–16
46. W. Wciślik and S. Lipiec, Void-Induced Ductile Fracture of Metals: Experimental Observations, *Materials (Basel)*, 2022, **15**(18), p 6473
47. V. Torres, R. Mayen-Mondragon, and J. Genesca, Assessment of the Galvanic Corrosion of Bi-Metallic Couple 7075-T6-Aluminum Alloy/Microalloyed Dual-Phase Steel, *Mater. Corros.*, 2022, **73**(6), p 940–949
48. T.A. Aeronautical, J. Jaquez-muñoz, C. Gaona-tiburcio, A. Lira-martinez, P. Zambrano-robledo, E. Maldonado-bandala, O. Samaniego-gamez, D. Nieves-mendoza, J. Olguin-coca, F. Estupiñan-lopez, and F. Almeraya-calderon, Susceptibility to Pitting Corrosion of Ti-CP2, Ti-6Al-2Sn-4Zr-2Mo, and Ti-6Al-4V Alloys for Aeronautical Applications, *Metals (Basel)*, 2021, **11**, p 1002
49. J. Dias Corpa Tardelli, C. Bolfarini, and A. Cândido dos Reis, Comparative Analysis of Corrosion Resistance between Beta Titanium and Ti-6Al-4V Alloys: A Systematic Review, *J. Trace Elem. Med. Biol.*, 2020, **62**, 126618. https://doi.org/10.1016/j.jtemb.2020.126618
50. J. Yang, H. Yang, H. Yu, Z. Wang, and X. Zeng, Corrosion Behavior of Additive Manufactured Ti-6Al-4V Alloy in NaCl Solution, *Metall. Mater. Trans. A Phys. Metall. Mater. Sci.*, 2017, **48**(7), p 3583–3593
51. K.T. Liu and J.G. Duh, Effect of Aluminum on the Corrosion Behavior of NiTiAl Thin Films, *Appl. Surf. Sci.*, 2007, **253**(12), p 5268–5273
52. A. Leon, G.K. Levy, T. Ron, A. Shirizly, and E. Aghion, The Effect of Hot Isostatic Pressure on the Corrosion Performance of Ti-6Al-4V Produced by an Electron-Beam Melting Additive Manufacturing Process, *Addit. Manuf.*, 2020, **33**, p 101039–101047. https://doi.org/10.1016/j.addma.2020.101039